

# Full- $f$ gyrokinetic simulation of turbulence in a helical open-field-line plasma

E. L. Shi,<sup>1,2</sup> G. W. Hammett,<sup>3, a)</sup> T. Stoltzfus-Dueck,<sup>3</sup> and A. Hakim<sup>3</sup>

<sup>1)</sup>Lawrence Livermore National Laboratory, Livermore, California 94550, USA

<sup>2)</sup>Department of Astrophysical Sciences, Princeton University, Princeton, New Jersey 08544, USA

<sup>3)</sup>Princeton Plasma Physics Laboratory, Princeton, New Jersey 08540, USA

(Dated: 24 October 2018)

Curvature-driven turbulence in a helical open-field-line plasma is investigated using electrostatic five-dimensional gyrokinetic continuum simulations in an all-bad-curvature helical-slab geometry. Parameters for a National Spherical Torus Experiment scrape-off-layer plasma are used in the model. The formation and convective radial transport of plasma blobs is observed, and it is shown that the radial particle-transport levels are several times higher than diffusive Bohm-transport estimates. By reducing the strength of the poloidal magnetic field, the profile of the heat flux to the divertor plate is observed to broaden.

## I. INTRODUCTION

Satisfactory and reliable quantitative predictions of turbulence and transport in the tokamak edge and scrape-off-layer (SOL) regions are widely believed to require the use of expensive gyrokinetic simulations in some capacity.<sup>1–4</sup> Some major outstanding questions that require numerical investigation include how the SOL power width is set,<sup>5–7</sup> how a confined plasma transitions from a low-confinement  $L$  mode to a high-confinement  $H$  mode,<sup>8,9</sup> and how high the  $H$ -mode pedestal temperature can get, since the pedestal temperature has a major impact on the core temperature profile and the resulting gain.<sup>10,11</sup> Gyrokinetic simulations in the edge and SOL regions are challenging for several reasons (e.g. large-amplitude fluctuations, steep profile gradients, closed and open magnetic field lines, X-point, effective sheath-model boundary conditions), but specialized particle-in-cell<sup>12,13</sup> and continuum gyrokinetic codes<sup>14–18</sup> have been making steady progress towards the ultimate goal as a predictive tool for boundary-plasma modeling. We refer the reader to Cohen and Xu<sup>1</sup> for a summary of early approaches to gyrokinetic edge and SOL simulation and Krommes<sup>19</sup> for an introduction to gyrokinetics. The particle-in-cell-based XGC1 code<sup>20</sup> is the only gyrokinetic code at present that is able to simulate turbulence in a three-dimensional diverted geometry. The first gyrokinetic simulations using continuum algorithms to simulate turbulence on straight open field lines were presented in Shi *et al.*<sup>14</sup> and then in Pan *et al.*<sup>16</sup> Here and in Shi<sup>15</sup>, we extend this earlier work to present the first gyrokinetic continuum simulations on open field lines including curved toroidal fields, which can strongly enhance the drive of plasma instabilities.

The SOL refers to the tokamak plasma region of open magnetic field lines between the last closed flux surface (LCFS) and the first wall. Here, the field lines intersect material surfaces that act as plasma sinks where the loss rate of electrons and ions are kept in approximate par-

ticle balance by a Debye sheath layer. Plasma-surface interactions<sup>21</sup> at the material interfaces can also contaminate the plasma with wall materials, which can severely degrade the fusion-plasma quality, but we do not yet incorporate these effects in the model being presented here.

Probe and imaging diagnostics have revealed the existence of intermittent coherent structures in the SOL referred to as *plasma filaments* or *blobs*,<sup>22–26</sup> which convectively transport particles, heat, momentum, and current across magnetic field lines.<sup>27</sup> Blobs are characterized by densities that are much higher than local background levels, a structure that is highly elongated along the magnetic field (much larger than the plasma minor radius), and much smaller scales perpendicular to the magnetic field,  $\sim 10\rho_i$ , where  $\rho_i$  is the ion gyroradius.<sup>27,28</sup> Cross-field transport in the far SOL is highly intermittent due to blob propagation<sup>28</sup> and is consequently poorly described in terms of effective diffusion coefficients and convective velocities.<sup>29</sup>

In a tokamak, the curvature and  $\nabla B$  forces are believed to set up a charge-separated dipole potential structure across the blob cross-section that results in its outward radial propagation via convective  $\mathbf{E} \times \mathbf{B}$  transport.<sup>27,30</sup> Finite-temperature effects of the blob can also cause spin motion if the blob is sheath-connected, which can reduce this radial motion.<sup>31</sup> Numerically, blobs dynamics have been studied using seeded-blob fluid simulations.<sup>32–35</sup> Self-consistent blob formation has been studied with two-dimensional models<sup>36–38</sup> and in three-dimensional turbulence simulations.<sup>12,39–41</sup>

The work presented here builds on our previous efforts in simulating open-magnetic-field-line turbulence in the Large Plasma Device<sup>42</sup> using the gyrokinetic continuum capabilities of the Gkeyll code.<sup>14</sup> In that study, the magnetic field was straight and uniform, and the plasma was highly collisional, which necessitated the use of an artificial electron-to-ion mass ratio ( $m_i/m_e = 400$ ) and reduced electron collision frequencies to make the simulations tractable, given the explicit algorithm used at present for the collision operator. Nevertheless, we found that our numerical approach based on discontinuous Galerkin methods and sheath-model boundary conditions for an open-field-line region were stable and pro-

<sup>a)</sup>hammett@pppl.gov

duced qualitatively reasonable results, which led to the first demonstration of open-field-line turbulence with a gyrokinetic continuum code. The reduced electron mass and collision-frequency restrictions have been relaxed for the simulations presented in this paper, which now also include a more sophisticated magnetic geometry.

We have added magnetic curvature and  $\nabla\mathbf{B}$  drifts to the Gkeyll code and can simulate a helical magnetic geometry approximating that in simple magnetized tori (SMT's), such as TORPEX<sup>43</sup> and Helimak.<sup>44</sup> In contrast to early work on the simulation of turbulence in SMT's based on the drift-reduced Braginskii equations and neglecting the ion temperature,<sup>45–47</sup> the gyrokinetic approach naturally can investigate plasmas with  $T_i \gtrsim T_e$ , which is commonly observed in the SOL.<sup>48–50</sup> Recent fluid simulations are also including finite  $T_i$ .<sup>51,52</sup>

Although our simulations do not yet simultaneously contain open- and closed-field-line regions,<sup>51–56</sup> we believe that many basic properties of SOL turbulence and transport are reproduced in this model. Additionally, the turbulence in this helical open-field-line geometry with parameters appropriate for a tokamak SOL has not been previously studied using a gyrokinetic PIC approach, either. We do acknowledge, however, that gyrokinetic PIC codes that have the necessary capabilities for the problem described in this paper have already been developed,<sup>12,13</sup> and it should be straightforward for these codes to implement this simple helical geometry for cross-code comparisons.

We discuss details of the helical-SOL model in Sec. II, including equations solved, simulation geometry, and boundary conditions. Additional details about the underlying algorithms can be found in Refs. 14 and 15. We present simulation results obtained using the Gkeyll code in Sec. III, such as heat-flux profiles, fluctuation statistics, and particle fluxes. Our conclusions are given in Sec. IV. To facilitate future code comparisons, we also present details of the initial conditions used in our simulations in Appendix A.

## II. MODEL

In the non-orthogonal field-aligned geometry used in the simulation,  $z$  measures distances along field lines relative to the midplane (poloidal angle  $\theta_{\text{pol}} = 0$  in a tokamak),  $x$  is the radial coordinate, and  $y$  is constant along a field line and measures distances perpendicular to field lines. The simulation geometry is a flux tube on the outboard side that wraps around the torus a specified number of times, terminating on material surfaces at each end in  $z$ . The resulting mapping from field-aligned coordinates  $(x, y, z)$  to standard cylindrical coordinates  $(R, \varphi, Z)$  is given by  $R = x$ ,  $Z = z \sin \theta$ , and  $\varphi = (y \sin \theta + z \cos \theta)/R_c$ , where  $R_c = R_0 + a$  and the field-line pitch  $\sin \theta = B_v/B$  are taken to be constant,  $R_0$  is the device major radius,  $a$  is the device minor radius, and  $B_v$  is the vertical (or poloidal) magnetic field.

This simple helical geometry has vertical flux surfaces (i.e., ignores flux expansion) and has no magnetic shear, and some further approximations to differential operators are made assuming short-wavelength turbulence for now. The final model nevertheless includes the main effect of the bad-curvature drive by toroidal magnetic fields while using an efficient field-aligned grid. See Refs. 57–59 and 15 for further details.

We solve a full- $f$  gyrokinetic equation written in the conservative form<sup>60–62</sup>

$$\frac{\partial \mathcal{J} f_s}{\partial t} + \nabla \cdot (\mathcal{J} \hat{\mathbf{R}} f_s) + \frac{\partial}{\partial v_{\parallel}} (\mathcal{J} \dot{v}_{\parallel} f_s) = \mathcal{J} C[f_s] + \mathcal{J} S_s \quad (1)$$

where  $f_s = f_s(\mathbf{R}, v_{\parallel}, \mu, t)$  is the gyrocenter distribution function for species  $s$ ,  $\mathcal{J} = B_{\parallel}^*$  is the Jacobian of the gyrocenter coordinates,  $B_{\parallel}^* = \mathbf{b} \cdot \mathbf{B}^*$ ,  $\mathbf{B}^* = \mathbf{B} + (Bv_{\parallel}/\Omega_s)\nabla \times \mathbf{b}$ ,  $C[f_s]$  represents the effects of collisions,  $\Omega_s = q_s B/m_s$ , and  $S_s = S_s(\mathbf{R}, v_{\parallel}, \mu, t)$  represents plasma sources. The characteristics are calculated as  $\hat{\mathbf{R}} = \{\mathbf{R}, H\}$  and  $\dot{v}_{\parallel} = \{v_{\parallel}, H\}$ , where the gyrokinetic Poisson bracket operator is

$$\{F, G\} = \frac{\mathbf{B}^*}{m_s B_{\parallel}^*} \cdot \left( \nabla F \frac{\partial G}{\partial v_{\parallel}} - \frac{\partial F}{\partial v_{\parallel}} \nabla G \right) - \frac{1}{q_s B_{\parallel}^*} \mathbf{b} \cdot \nabla F \times \nabla G, \quad (2)$$

and the gyrocenter Hamiltonian is  $H_s = \frac{1}{2} m_s v_{\parallel}^2 + \mu B + q_s \phi$ , where the long-wavelength limit has been taken to neglect gyroaveraging. A conservative Lenard–Bernstein collision operator<sup>63</sup> that neglects the velocity dependence of the collision frequency is used to model self-species and electron–ion collisions.

This system is closed by the long-wavelength gyrokinetic Poisson equation with a linearized ion polarization density

$$-\nabla_{\perp} \cdot \left( \frac{n_{i0}^g q_i^2 \rho_{s0}^2}{T_{e0}} \nabla_{\perp} \phi \right) = \sigma_g = q_i n_i^g(\mathbf{R}) - e n_e(\mathbf{R}), \quad (3)$$

where  $\rho_{s0} = c_{s0}/\Omega_i$ ,  $c_{s0} = \sqrt{T_{e0}/m_i}$ , and  $n_{i0}^g$  is the background ion gyrocenter density that we take to be a constant in space and in time.

In these equations, we neglect geometrical factors arising from a cylindrical coordinate system everywhere except in  $\mathbf{B}^* = \mathbf{B} + (Bv_{\parallel}/\Omega_s)\nabla \times \mathbf{b}$ , where we make the approximation that perpendicular gradients are much stronger than parallel gradients:

$$\begin{aligned} (\nabla \times \mathbf{b}) \cdot \nabla f(x, y, z) &= [(\nabla \times \mathbf{b}) \cdot \nabla y] \frac{\partial f(x, y, z)}{\partial y} \\ &\quad + [(\nabla \times \mathbf{b}) \cdot \nabla z] \frac{\partial f(x, y, z)}{\partial z} \\ &\approx [(\nabla \times \mathbf{b}) \cdot \mathbf{e}^y] \frac{\partial f(x, y, z)}{\partial y}. \end{aligned} \quad (4)$$

Here, we assume that  $(\nabla \times \mathbf{b}) \cdot \mathbf{e}^y = -1/x$ , where  $\mathbf{e}^y = \nabla y$  is a ‘co-basis’ direction. This type of approximation has also been employed in some fluid simulations of SMT's.<sup>46,64</sup> We assume that  $\mathbf{B} = B_{\text{axis}}(R_0/x)\mathbf{e}_z$ .

Periodic boundary conditions are applied to both  $f$  and  $\phi$  in  $y$ , and the Dirichlet boundary condition  $\phi = 0$

is applied in  $x$ , which prevents gyrocenters from crossing the surfaces in  $x$ . Conducting-sheath boundary conditions are applied to  $f$  in  $z$ , which partially reflect gyrocenters of one species and fully absorb gyrocenters of the other species into the wall depending on the sign of the sheath potential. The potential is determined by solving the gyrokinetic Poisson equation [Eq. (3)]. Evaluating this potential at the sheath entrances (the ends of the simulation domain in  $z$ ) gives the sheath potential, which is used to determine which particles are reflected by the sheath. This is the gyrokinetic analog of how fluid codes have used the vorticity to calculate the potential and sheath effects (for example, see Ricci and Rogers<sup>46</sup>). We refer to these boundary conditions as conducting-sheath boundary conditions<sup>14,15</sup> because they allow self-consistent currents locally in and out of the end plates. This is in contrast to the logical-sheath boundary-condition model,<sup>65–67</sup> which assumes an insulating sheath with zero current density at the end plates everywhere. There is no closed-field-line region in our present model.

We use parameters roughly approximating a singly ionized H-mode deuterium plasma in the NSTX SOL:<sup>68,69</sup>  $n_{70}^0 = 7 \times 10^{18} \text{ cm}^{-3}$ ,  $T_e \sim 40 \text{ eV}$ ,  $T_i \sim 60 \text{ eV}$ ,  $B_{\text{axis}} = 0.5 \text{ T}$ ,  $R_0 = 0.85 \text{ m}$ ,  $a_0 = 0.5 \text{ m}$ . Although we use parameters for an H-mode plasma, we do not attempt or claim to capture H-mode physics (e.g. an edge transport barrier) in our simulations, since they include only the SOL and not the pedestal.

The simulation box has dimensions  $L_x = 50\rho_{s0} \approx 14.6 \text{ cm}$ ,  $L_y = 100\rho_{s0} \approx 29.1 \text{ cm}$ ,  $L_z = L_p/\sin\theta$ , where  $L_p = 2.4 \text{ m}$ ,  $\rho_{s0} = c_{s0}/\Omega_i$ , and  $\theta$  is the magnetic-field-line incidence angle. The magnetic field is taken to be comprised primarily of a toroidal component with a smaller vertical component (referred to as  $B_v$ ), resulting in a helical-field-line geometry that roughly approximates the tokamak SOL. We present results with  $\sin\theta = B_v/B_z = (0.2, 0.3, 0.6)$  in Sec. III, which correspond to  $L_z = (12, 8, 4) \text{ m}$ . The connection length to the divertor plate in the real NSTX experiment is typically quite long, over 10 m, but we consider smaller values that might represent the shorter connection length from the midplane to the X-point region, where the magnetic shear is very strong. In this study, the magnetic-field-line incidence angle is not accounted for in the sheath boundary conditions (i.e. no Chodura sheath<sup>70</sup>).

We use an energy-conserving discontinuous Galerkin method for the spatial discretization of the equations, which is a generalization of the algorithm of Liu & Shu<sup>71</sup> for two-dimensional incompressible flow in the vorticity–stream function formulation. Time discretization is performed using an explicit third-order strong-stability-preserving Runge–Kutta algorithm.<sup>72</sup> The positivity of the distribution function is not automatically guaranteed in our algorithms, and our method to keep  $f > 0$  results in the addition of a small amount of numerical heating  $\sim 10\%$  of the source power to the system. The details of the numerical algorithms, energy conser-

vation, and sheath boundary conditions are discussed in Refs. 14 and 15.

The position-space extents are  $x \in [R_0 + a_0 - L_x/2, R_0 + a_0 + L_x/2]$ ,  $y \in [-L_y/2, L_y/2]$ ,  $z \in [-L_z/2, L_z/2]$ , and the velocity-space extents are  $v_{\parallel s} \in [-v_{\parallel s, \text{max}}, v_{\parallel s, \text{max}}]$ , where  $v_{\parallel s, \text{max}} = 4v_{ts} = 4\sqrt{T_s/m_s}$  and  $\mu_{s, \text{max}} = (3/4)m_s v_{\parallel s, \text{max}}^2/(2B_0)$ , where  $B_0 = B_{\text{axis}}R_0/(R_0 + a_0)$ . The solution in each cell is expanded using piecewise-linear basis functions, i.e. the span of monomials in the five phase-space variables with each variable degree  $\leq 1$ . This choice results in 32 degrees-of-freedom per element to represent the distribution function and Hamiltonian. The grid resolution is  $(N_x, N_y, N_z, N_{v_{\parallel}}, N_{\mu}) = (18, 36, 10, 10, 5)$ , and a uniform grid spacing is used.

The plasma density source has the following form:

$$S(x, z) = \begin{cases} S_0 \max \left[ \exp \left( \frac{-(x-x_S)^2}{2\lambda_S^2} \right), 0.1 \right], & |z| < L_z/4 \\ 0 & \text{else,} \end{cases} \quad (5)$$

where  $x_S = -0.05 \text{ m} + R_0 + a_0$ ,  $\lambda_S = 5 \times 10^{-3} \text{ m}$ , and  $S_0$  is chosen so that the source has total (electron plus ion) power  $P_{\text{source}} = 0.27L_z/L_{z0} \text{ MW}$ , where  $L_{z0} = 4 \text{ m}$ . The expression for the source power comes from multiplying  $P_{\text{SOL}} = 5.4 \text{ MW}$ , the total power into the SOL, by the fraction of the total device volume covered by the simulation box. A floor of  $0.1S_0$  is used in the  $|z| < L_z/4$  region to prevent regions of  $n \ll n_0$  from developing at large  $x$ , which can result in distribution-function positivity issues. The distribution function of the sources are non-drifting Maxwellians with a temperature profile  $T_{e,i} = 74 \text{ eV}$  for  $x < x_S + 3\lambda_S$  and  $T_{e,i} = 33 \text{ eV}$  for  $x \geq x_S + 3\lambda_S$ . These choices result in an integrated source particle rate of  $\approx 9.6 \times 10^{21} \text{ s}^{-1}$  for the  $L_z = L_{z0}$  ( $B_v/B_z = 0.6$ ) case.

We do not yet include a closed-field-line region in our simulations, so we only simulate a SOL. The  $x < x_S + 3\lambda_S$  region will be referred to as the source region in this paper, while the  $x \geq x_S + 3\lambda_S$  region will be referred to as the SOL region. We can think of the  $x = x_S + 3\lambda_S$  location as the LCFS.

### III. SIMULATION RESULTS

Starting from an initial condition estimated by the steady-state solution of one-dimensional fluid equations (see Appendix A), the sources steepen the plasma profiles, quickly triggering curvature-driven modes that grow on a timescale comparable to  $\gamma \sim c_s/\sqrt{R}\lambda_p$ . We emphasize that our system does not contain ballooning modes since there are no ‘good-curvature’ regions. As shown in Fig. 1, radially elongated structures extending far from the source region are generated and subsequently broken up by sheared flows in the  $y$  direction in the source region, leaving radially propagating blobs in the SOL region. Using the time-averaged profiles from the

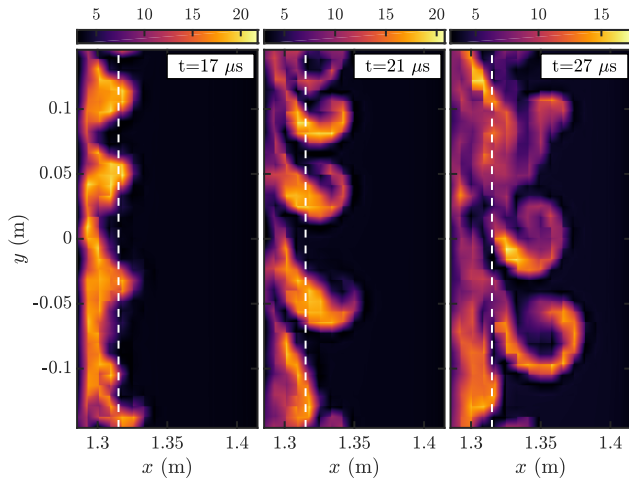


FIG. 1. Snapshots of the electron density (in  $10^{18} \text{ m}^{-3}$ ) at various times ( $t = 17 \mu\text{s}$ ,  $21 \mu\text{s}$ , and  $27 \mu\text{s}$ ) near the beginning of a simulation in the perpendicular  $x$ - $y$  plane at  $z = 0 \text{ m}$ . This simulation has  $B_v/B_z = 0.3$ . The dashed line indicates the boundary between the source and SOL regions. Note that each plot uses a different color scale to better show the features.

same  $B_v/B_z = 0.3$  ( $L_z = 8 \text{ m}$ ) simulation, we estimate  $\gamma \sim 1.9 \times 10^5 \text{ s}^{-1}$  using  $\lambda_p \approx 2.9 \text{ cm}$ ,  $T_e \approx 30 \text{ eV}$ , and  $R = x_S = 1.3 \text{ m}$ . On a time scale long compared to  $\gamma^{-1}$  and  $\tau_i = (L_z/2)/v_{ti} \sim 50 \mu\text{s}$ , the conducting-sheath boundary conditions maintain a quasi-steady state in which the particle losses to the end plates are balanced by the plasma sources. Snapshots of the electron density, electron temperature, and electrostatic potential from the quasi-steady state ( $t = 625 \mu\text{s}$ ) for the  $B_v/B_z = 0.3$  case are shown in Fig. 2.

For the steepest magnetic-field-line-pitch case ( $B_v/B_z = 0.6$ ), we performed a second simulation with magnetic-curvature effects removed, keeping all other parameters unchanged. The resulting magnetic geometry consists only of straight magnetic field lines, so coherent structures of elevated plasma density cannot become polarized by curvature forces. As shown in the electron-density snapshot comparison in Fig. 3, the presence of magnetic curvature appears to have an important role in the turbulent dynamics of the system. When magnetic-curvature effects are removed, the radial propagation of coherent structures into the SOL region appears to be significantly weakened or absent, and most of the density is localized to the source region.

Figure 4 compares radial profiles of the background electron densities, normalized electron-density fluctuation levels, and radial  $E \times B$  particle fluxes  $\Gamma_{n,r}$  between these two simulations. The radial particle flux due to electrostatic turbulence is calculated as  $\Gamma_{n,r} = \langle \tilde{n}_e \tilde{v}_r \rangle$ ,<sup>28</sup> where  $v_r = E_y/B$  and the brackets  $\langle \dots \rangle$  indicate an average over a period that is long compared to the fluctuation time scale and an average over  $y$  and the central region in  $z$ ,  $-0.5 \text{ m} < z < 0.5 \text{ m}$ . The fluctuation of a time-

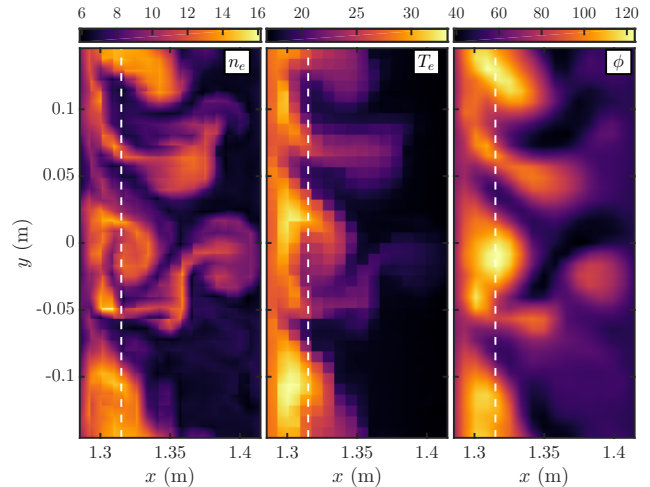


FIG. 2. Snapshots of the electron density (in  $10^{18} \text{ m}^{-3}$ ), electron temperature (in eV), and electrostatic potential (in V) in the plane perpendicular to the magnetic field at  $z = 0 \text{ m}$ . This plot is made at  $t = 625 \mu\text{s}$ , which is after several ion transit times ( $\tau_i \sim 50 \mu\text{s}$ ). This simulation has  $B_v/B_z = 0.3$ . The dashed line indicates the boundary between the source and SOL regions. A mushroom structure in the electron density is observed at large  $x$ .

varying quantity  $A$  is denoted as  $\tilde{A}$ , which is related to the total  $A$  as  $\tilde{A} = A - \langle A \rangle_t$ . Here, the brackets  $\langle \dots \rangle_t$  indicate an average in time. Notable differences between these two simulations are found in all three quantities plotted. Compared to the helical-SOL simulation, the straight-field-line simulation has a background density profile that decays more rapidly, fluctuation levels that quickly drop to  $\approx 0\%$  outside  $x \approx 1.35 \text{ m}$ , and a  $\approx 2.5$  times smaller  $\Gamma_{n,r}$  that also drops to approximately zero outside  $x \approx 1.34 \text{ m}$ .

We have also performed a scan of the mass ratio  $m_i/m_e$  from the actual ratio of 3698 down to 100 (by increasing the electron mass), and we observed no significant quantitative or qualitative changes in the turbulence. The mass ratio might play an important role in a different parameter regime, however.

Effects connected to  $B_v \sim B_p \sim I_{\text{plasma}}$  are explored by changing the magnetic-field-line incidence angle, since  $\sin \theta = B_v/B_z$ . We have performed simulations at three values of magnetic-field-line pitches  $B_v/B_z = (0.2, 0.3, 0.6)$ , which correspond to  $L_z = (12, 8, 4) \text{ m}$  and  $\theta = (20.14^\circ, 30.47^\circ, 64.4^\circ)$ . We scale the source appropriately in each simulation to keep the volumetric source rate the same. In all these simulations, the source is localized to the  $z \in [-L_z/4, L_z/4]$  region to model a source with a fixed poloidal extent. As  $\theta$  is decreased, the plasma profiles are observed to become less peaked, implying that turbulence transport in the  $x$ -direction increased with decreasing  $\theta$ .

We calculate the steady-state parallel heat flux  $q = \sum_s \int d^3v H_s v_{\parallel} f_s$  at the sheath entrance and average  $q$



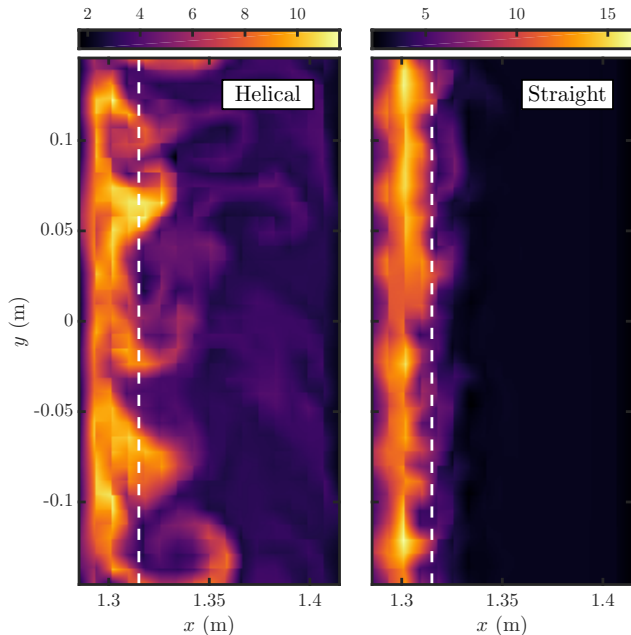


FIG. 3. Comparison of an electron density snapshot (in  $10^{18} \text{ m}^{-3}$ ) between a simulation in a helical-magnetic-field-line geometry and a simulation in a straight-magnetic-field-line geometry with  $B = B_0$ . The formation of blobs in the helical-SOL simulation results in the transport of density to large  $x$  and a broad density profile. Coherent structures of elevated plasma density do not appear to convect to large  $x$  in the straight-magnetic-field-line case, and so density is mostly localized to the source region. The plots are made in the perpendicular  $x$ - $y$  plane at  $z = 0$  m and  $t = 681 \mu\text{s}$ . The dashed line indicates the boundary between the source and SOL regions. Note that each plot uses a different color scale to better show the features.

in the  $y$ -direction to obtain a radial profile of the steady-state parallel heat flux for each case. To compare the heat fluxes on an equal footing, we plot the component of the parallel heat flux normal to the divertor plate  $q_{\perp} = q \sin \theta$  in Fig. 5. Compared to the  $B_v/B_z = 0.6$  case, the heat-flux profiles for the cases with a shallower pitch are much broader. This behavior is consistent with the observation in tokamaks that the SOL heat-flux width is inversely proportional to the poloidal magnetic field (analogous to  $B_v$  in this model) and the plasma current,<sup>5,73</sup> although the physical reasons behind the scaling in our model and in a tokamak SOL may be quite different. We note that a significant amount of plasma in the smallest  $\theta$  case gets near the outer radial wall, where further radial transport is suppressed, since the outer boundary is taken to be an ideal conducting plate with constant  $\phi$ , so the  $\mathbf{E} \times \mathbf{B}$  velocity into the side walls,  $\propto \partial\phi/\partial y$ , vanishes. Simulations with a larger domain extent in the  $x$  coordinate (and/or finite-Larmor-radius effects in the collision operator to include classical transport to the side wall) might exhibit more of an exponential fall off over a wider radial range, further reducing the density in the right-hand side

of the simulation.

The broad heat-flux profiles in Fig. 5 can be connected to the increased outward radial turbulent transport as  $B_v/B_z$  becomes shallower. We compute the steady state radial particle flux  $\Gamma_{n,r}$  near the midplane in the region  $-0.5 \text{ m} < z < 0.5 \text{ m}$  for each value of  $B_v/B_z$  and plot the  $y$ -averaged fluxes in Fig. 6 (solid lines). Since the simulation box occupies a larger fraction the device volume as  $B_v/B_z$  is decreased, but the source occupies the same fraction of the simulation box and has a fixed volumetric source rate, the background density levels increase as  $B_v/B_z$  decreases. Another way to say this is that with a fixed volumetric source density (fixed in particles per cubic meter per second), the mean density is expected to increase as the parallel connection length  $L_z/2$  increases and the parallel loss rate  $\sim 1/\tau_i = 2v_{ti}/L_z$  decreases. Therefore, the magnitude of the  $\Gamma_{n,r}$  profiles in Fig. 6 should not be taken alone as a measure of turbulence levels.

The  $\Gamma_{n,r}$  profiles can be compared with the radial particle fluxes that result from assuming Bohm diffusion, i.e.  $\Gamma_B = D_B \partial_x n_e$ , where the diffusion coefficient  $D_B = (1/16)k_B T_e / (eB)$ . In the  $x > 1.36$  m region,  $\Gamma_{n,r}/\Gamma_B \approx 16$  for the  $B_v/B_z = 0.2$  case, while  $\Gamma_{n,r}/\Gamma_B \approx 8$  for the  $B_v/B_z = 0.6$  case. One might expect the maximum level of turbulent transport to be comparable to the levels set by  $D_B$ , but it is important to remember that  $D_B$  is a *diffusive* transport estimate. The *convective* transport of blobs in these simulations appears to be responsible for the much-higher turbulent fluxes. Experimental data from tokamaks also suggest that the higher-than-Bohm particle transport in the SOL is due to the non-diffusive transport of blobs.<sup>28,74</sup>

Density fluctuation statistics are often of interest in the SOL to characterize the turbulence. Considering again a time-varying quantity  $A$ , we define the skewness of  $A$  as  $E[\tilde{A}^3]/\sigma^3$  and the excess kurtosis of  $A$  as  $E[\tilde{A}^4]/\sigma^4 - 3$ , where  $\sigma$  is the standard deviation of  $A$  and  $E[\dots]$  denotes the expected value. Figure 7 shows the radial profiles of the normalized fluctuation level, skewness, and excess kurtosis for electron-density fluctuations and electrostatic-potential fluctuations computed near the  $z = 0$  m plane. The density and potential fluctuations are normalized to their local background values. The positive skewness and excess kurtosis values are signatures of intermittency, which indicates an enhancement of large-amplitude positive-density-fluctuation events and is connected to the transport of blobs.<sup>28,75</sup>

A somewhat counter-intuitive result is the reduction of density fluctuation levels as  $B_v/B_z$  is decreased, given that Figs. 5 and 6 indicate that turbulent spreading is increased as  $B_v/B_z$  is decreased. The skewness and excess kurtosis plots in Fig. 7 indicate that the density fluctuations become closer to a normal distribution as  $B_v/B_z$  is decreased. These trends in the density fluctuation statistics can be understood by noting that the background density profile becomes less peaked and more uniform in the  $x$ -direction as  $B_v/B_z$  is decreased, so a blob that is

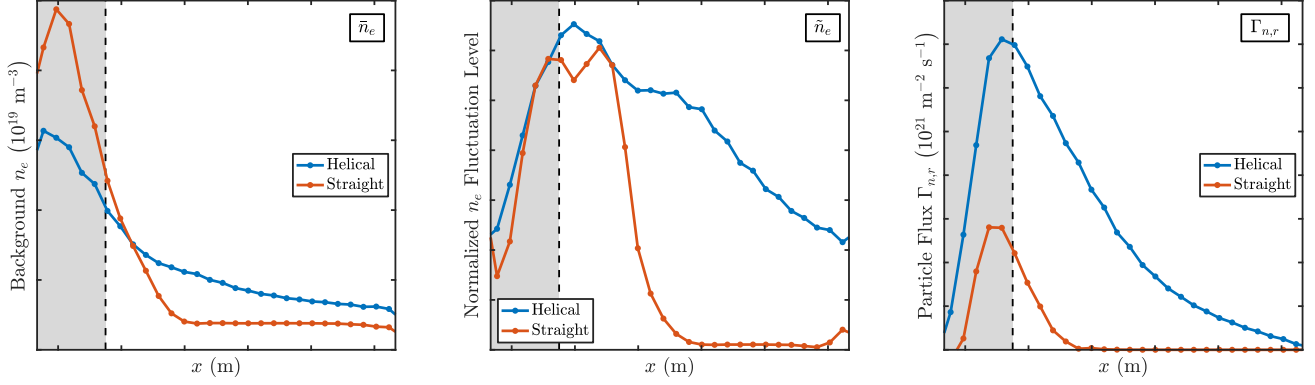


FIG. 4. Radial profiles of the background electron densities (in  $10^{19} \text{ m}^{-3}$ ), normalized electron-density fluctuation levels, and radial  $E \times B$  particle fluxes  $\Gamma_{n,r}$  (in  $10^{21} \text{ m}^{-2} \text{ s}^{-1}$ ) for a helical SOL simulation and a straight-field-line simulation with  $B = B_{\text{axis}}$ . These plots are computed using data near the midplane in the region  $-0.5 \text{ m} < z < 0.5 \text{ m}$  and sampled at  $0.25 \mu\text{s}$  intervals over a  $\sim 400 \mu\text{s}$  period. The shaded area indicates the region in which the source is concentrated. The background density profile in the straight-field-line simulation does not decay to 0 at large  $x$  due to the presence of a constant low-amplitude source in that region to help mitigate positivity issues with the distribution function.

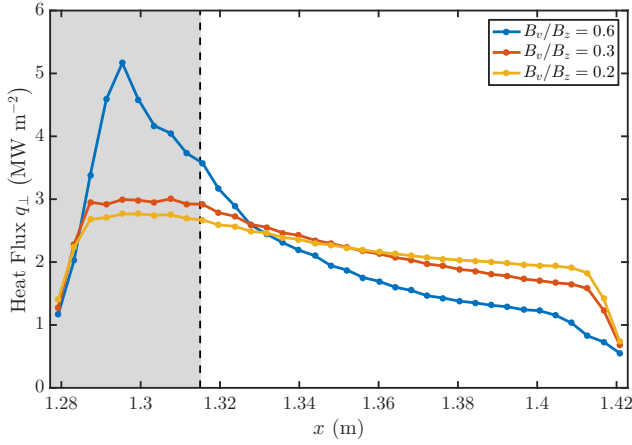


FIG. 5. Comparison of the steady-state parallel heat flux normal to the divertor plate for three cases with different magnetic-field-line pitches. The shaded area indicates the region in which the source is concentrated. The heat-flux profile is observed to broaden as  $B_v/B_z$  is decreased. Since a large amount of plasma gets near the outer radial boundary, where further radial transport is suppressed by the  $\phi = 0$  constant ideal-conducting-wall condition, the profiles in the shallower-pitch cases may exhibit more of a uniform exponential fall off by increasing the box size in the radial direction.

formed in the source region propagating in the SOL has a density that is closer to the background level, which results in lower relative fluctuation, skewness, and excess kurtosis values when compared to the large  $B_v/B_z$  case. Additionally, the density flux is constrained by the use of a fixed volumetric source rate, so as the background density increases with decreasing  $B_v/B_z$ , the relative density fluctuation levels tend to decrease. We also observe that the potential fluctuations are much less intermittent than the density fluctuations at the same  $B_v/B_z$ . This obser-

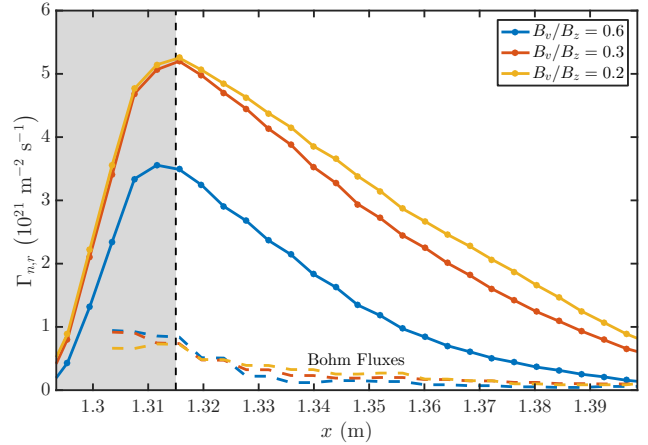


FIG. 6. Comparison of the radial  $E \times B$  particle flux evaluated near the midplane for three cases with different magnetic-field-line pitches. The shaded area indicates the region in which the source is concentrated. The dashed lines are Bohm-flux estimates for comparison.

vation could be a real, physical effect, but we note that the fact that the temperature at large  $x$  runs into the grid resolution (the lowest temperature that can be represented on the velocity grid) could be influencing the potential fluctuation statistics in this region. Unlike the density fluctuations, the normalized potential fluctuation levels tend to increase with decreasing  $B_v/B_z$ .

Figure 8 shows radial profiles of the steady-state ion and electron temperatures and ion-to-electron temperature ratios near the midplane for different  $B_v/B_z$ . For all three simulations,  $T_i/T_e$  falls in the range 1.5–2, which is within the range of 1–10 that is observed a few centimeters outside the LCFS in tokamaks.<sup>49</sup> Similar to the heat-flux profiles shown in Fig. 5, the profiles are steepest

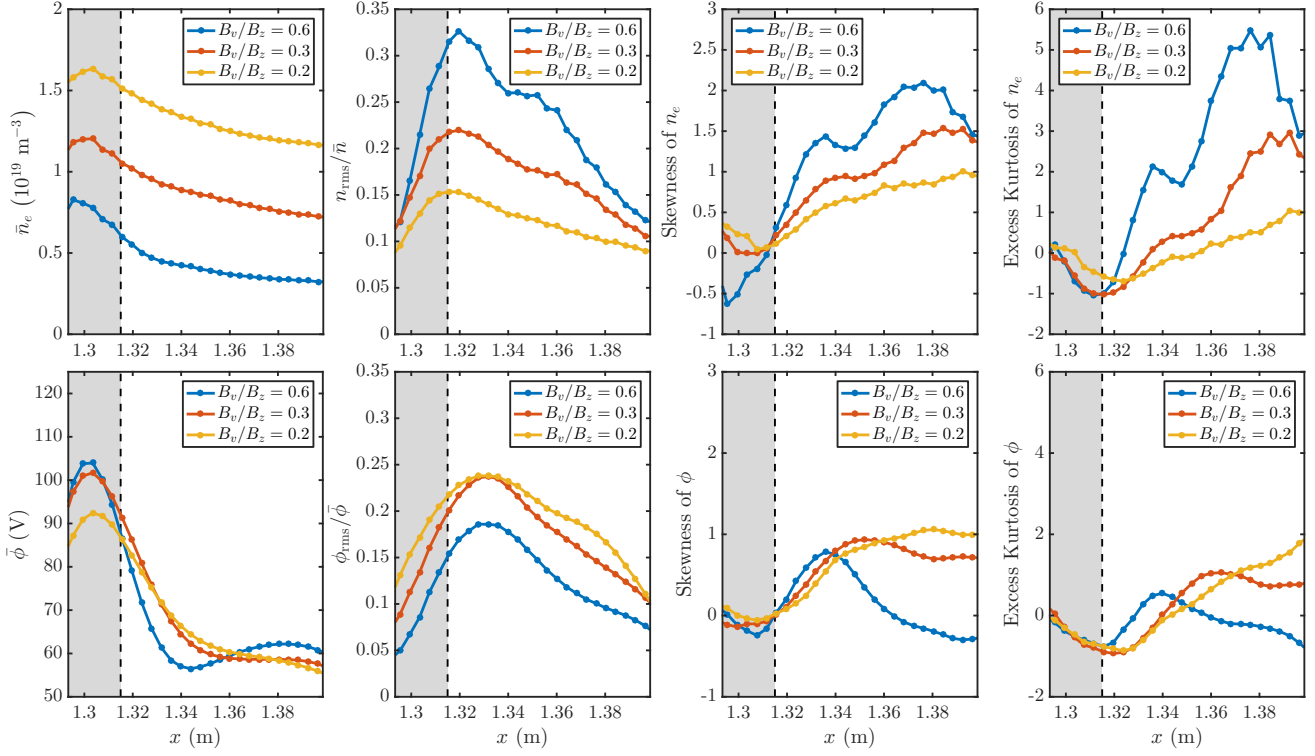


FIG. 7. Comparison of the electron-density fluctuation statistics (top row) and electrostatic-potential fluctuation statistics (bottom row) computed near the  $z = 0$  m plane for three cases with different magnetic-field-line pitches. The potential fluctuations are notably less intermittent than the density fluctuations. The shaded area indicates the region in which the source is concentrated.

for the case with  $B_v/B_z = 0.6$  and decay more gradually in the lower  $B_v/B_z$  cases. SOL measurements typically show that the ratio  $T_i/T_e$  increases with radius.<sup>49</sup> We see this trend in Fig. 8 for  $B_v/B_z = 0.3$  and  $0.2$ , but not for  $B_v/B_z = 0.6$ . This reversed trend for  $B_v/B_z = 0.6$  is likely connected to the relatively flat  $T_e$  in the  $B_v/B_z = 0.6$  case, the low-amplitude source of  $\sim 33$  eV electrons at large  $x$  [see the form of the plasma source, Eq. (5)] could be setting  $T_e$  in this region.

The flat  $T_e$  at large  $x$  could also be an artifact from the electrons running into a floor in the temperature at large  $x$ . However, we note that the minimum electron temperature allowed on our present grid is  $T_{e,\min} = (2/3)T_{\perp e,\min} + (1/3)T_{\parallel e,\min} = 11$  eV based on  $T_{\perp e,\min} = 16$  eV and  $T_{\parallel e,\min} = 1.1$  eV, which is somewhat lower than the  $T_e$  seen in this region. We can test this in future work by running higher-resolution runs, including a variable  $\mu$  grid to better resolve low energies or by using exponential reconstructions, which is currently being added to the code.

The normalized root-mean-square (r.m.s.) electron-density fluctuation level in the  $x$ - $z$  plane is shown in Fig. 9. For all three values of  $B_v/B_z$ , the density fluctuation levels are the largest in the source region  $|z| < L_z/4$ . The normalized density fluctuation levels in the  $B_v/B_z = 0.6$  case are fairly uniform along the field

lines, while they tend to fall off by about a factor of 2–3 towards the sheaths in the smaller  $B_v/B_z$  cases. This effect could be a result of the stronger influence of the sheath on the potential as the distance from the source to the sheath is decreased. The instantaneous snapshots of  $\tilde{n}_e$  (not shown) indicate a strong  $k_{\parallel} = 0$  component for the largest  $B_v/B_z$  cases, while more parallel structure is apparent in the smaller  $B_v/B_z$  cases.

The fluctuation statistics can also give information about the strength of the electron adiabatic response for each simulation. By assuming that the electrons are isothermal along field lines, parallel force balance satisfies

$$-n_e e E_{\parallel} - \nabla_{\parallel} P_e = 0 \quad (6)$$

$$-n_e e E_{\parallel} = T_e \nabla_{\parallel} n_e \quad (7)$$

$$\frac{e \nabla_{\parallel} \phi}{T_e} = \nabla_{\parallel} \ln n_e \quad (8)$$

$$\frac{e \phi_{\text{mid}}}{T_e} = \frac{e \phi_{\text{sh}}}{T_e} + \ln \left( \frac{n_{\text{mid}}}{n_{\text{sh}}} \right), \quad (9)$$

where  $\phi_{\text{sh}}$  and  $n_{\text{sh}}$  are the electrostatic potential and electron density evaluated at the sheath entrances and  $\phi_{\text{mid}}$  and  $n_{\text{mid}}$  are the same quantities, but evaluated at the midplane ( $z = 0$  m). To compute the cross-coherence diagnostic,<sup>53,77,78</sup> ordered pairs  $(e \phi_{\text{mid}}/T_e, e \phi_{\text{sh}}/T_e + \ln(n_{\text{mid}}/n_{\text{sh}}))$  falling in the region  $1.318 \text{ m} \leq x \leq$

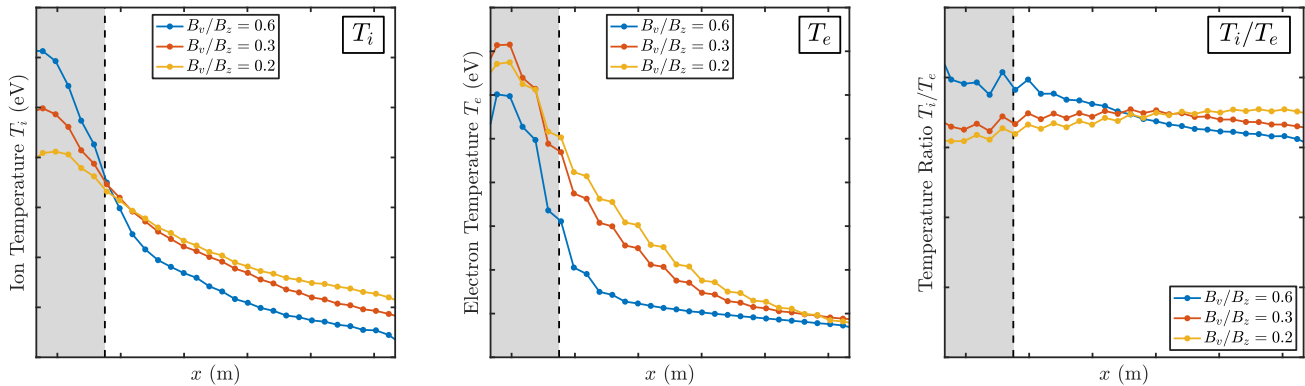


FIG. 8. Radial profiles of the steady-state ion and electron temperatures near the midplane and ion-to-electron temperature ratios for cases with different magnetic-field-line pitches. Although both electrons and ions are sourced at the same temperature, the sheath allows high-energy electrons to be rapidly lost from the system, resulting in lower electron temperatures in the SOL if collisions are not rapid enough to equilibrate the two species.<sup>49,76</sup>

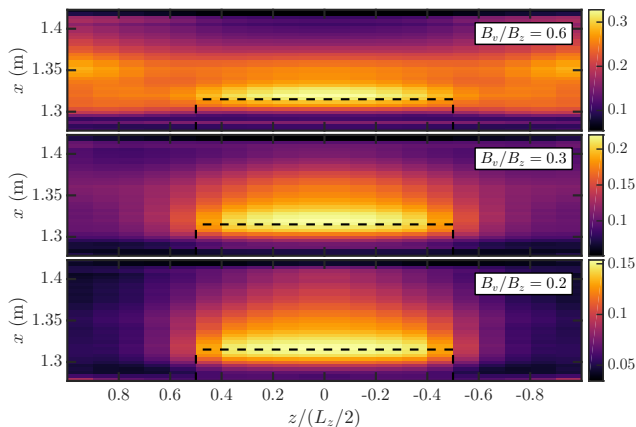


FIG. 9. Comparison of the parallel structure of the normalized r.m.s. electron-density fluctuation amplitude for three cases with different magnetic-field-line pitches. While the density fluctuations are primarily  $k_{\parallel} = 0$  in the  $B_v/B_z = 0.6$  case, more parallel structure is observed in the lower  $B_v/B_z$  cases. The region in which the source is concentrated is indicated by the dashed black lines.

1.326 m (approximately where the maximum density and potential fluctuations are) are sampled at  $1 \mu\text{s}$  intervals over a  $\sim 1$  ms period for each simulation. Figure 10 shows the resulting plots (normalized bivariate histograms), which all indicate a strong correlation between the two sides of Eq. (9), and so the electrons are strongly adiabatic, meaning that the electron distribution function along a field line closely follows a Boltzmann distribution.<sup>79</sup> This finding indicates that it might be possible to obtain similar results using a two-dimensional turbulence model (with reduced parallel dynamics and sheath-model boundary conditions) for the parameters considered here. To quantify the degree of

non-adiabaticity, we define the parameter

$$\epsilon_{\text{na}}^2 = \frac{E \left( (\bar{\phi}_{\text{mid}} - \bar{\phi}_{\text{ad}})^2 \right)}{E \left( [\bar{\phi}_{\text{mid}} - E(\bar{\phi}_{\text{mid}})]^2 \right)}, \quad (10)$$

where  $\bar{\phi}_{\text{mid}}$  is the left-hand side of Eq. (9) and  $\bar{\phi}_{\text{ad}}$  is the right-hand side of Eq. (9). The  $\epsilon_{\text{na}}$  parameter measures the fraction of fluctuations in  $\phi$  that are due to non-adiabatic effects. We find that  $\epsilon_{\text{na}}$  is 0.094 for  $B_v/B_z = 0.6$ , 0.226 for  $B_v/B_z = 0.3$ , and 0.310 for  $B_v/B_z = 0.2$ , which is consistent with our expectation that the electrons become less adiabatic as  $B_v/B_z$  is decreased.

Figure 11(a) shows the radial profile of the autocorrelation time  $\tau_{\text{ac}}$  (computed from time traces of the density fluctuations). In the SOL of the simulation,  $\tau_{\text{ac}}$  tends to increase with radius, which is a trend observed in measurements on NSTX (see Fig. 12 of Zweben *et al.*<sup>68</sup>). The autocorrelation time for the  $B_v/B_z = 0.2$  and  $B_v/B_z = 0.3$  cases is found to vary between  $\sim 5 \mu\text{s}$  and  $\sim 9 \mu\text{s}$ , while the autocorrelation time for the  $B_v/B_z = 0.6$  case exhibits a larger variation in the SOL, with  $\tau_{\text{ac}} \approx 4 \mu\text{s}$  for  $x < 1.34$  m and increasing to  $\approx 12 \mu\text{s}$  at the outer radial boundary. The autocorrelation times we observe in our simulations are lower than the  $\tau_{\text{ac}} \sim 10\text{--}40 \mu\text{s}$  reported by Zweben *et al.*<sup>68</sup> for the NSTX edge and SOL, but are well within the  $\tau_{\text{ac}} \sim 2\text{--}20 \mu\text{s}$  range that is typical for edge and SOL turbulence in other tokamaks.<sup>28,48</sup>

Figure 11(b) shows the poloidal and radial correlation lengths ( $L_{\text{pol}}$  and  $L_{\text{rad}}$  respectively) using the electron-density fluctuations near the  $z = 0$  m plane. The correlation length at a radial location is obtained by averaging the correlation length computed at several points in  $y$ . At an individual point, the correlation length is determined from the correlation function, which is constructed by computing the equal-time two-point autocorrelation function for density fluctuations separated by some distance  $\Delta y$  for  $L_{\text{pol}}$  or  $\Delta x$  for  $L_{\text{rad}}$ . Having observed a



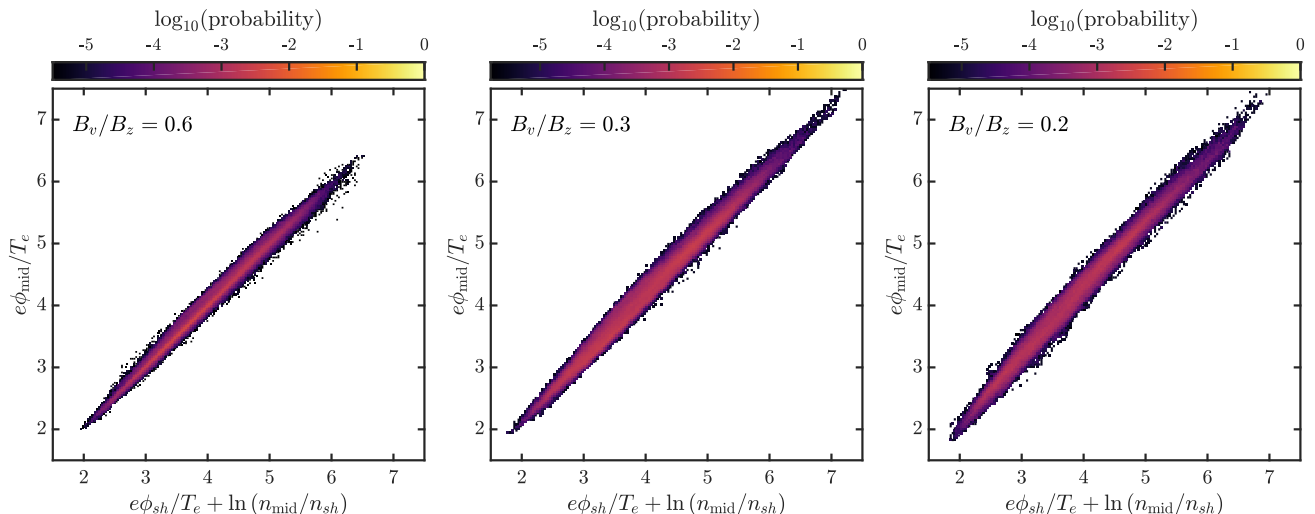


FIG. 10. Comparison of the cross-coherence between the midplane potential  $e\phi_{\text{mid}}/T_e$  and  $e\phi_{\text{sh}}/T_e + \ln(n_{\text{mid}}/n_{\text{sh}})$  [see Eqs. (6)–(9)] for three cases with different magnetic-field-line pitches  $\theta$ . Here,  $\phi_{\text{sh}}$  is the sheath potential,  $n_{\text{mid}}$  is the midplane electron density, and  $n_{\text{sh}}$  is the sheath electron density. These plots are created by binning ordered pairs of the two quantities sampled every  $0.25 \mu\text{s}$  over a  $\sim 1 \text{ ms}$  time interval at solution nodes falling in the region  $1.318 \text{ m} \leq x \leq 1.326 \text{ m}$ . In all three cases, the two quantities are highly correlated, which indicates that the electrons are strongly adiabatic (near parallel force balance).

significant wave feature in the poloidal correlation function, we determined  $L_{\text{pol}}$  by fitting the poloidal correlation function to  $e^{-|\Delta y|/L_{\text{pol}}} \cos(k_{\text{wave}}\Delta y)$ . The radial correlation function, which does not have a wave feature, is computed using the full width at half maximum (FWHM) as  $L_{\text{rad}} = \text{FWHM}/(2 \ln 2)$ .

For all three values of  $B_v/B_z$ , we observe that the ratio  $L_{\text{pol}}/L_{\text{rad}}$  is between 1.2 and 1.6 for most of the radial domain, which is similar to the  $L_{\text{pol}}/L_{\text{rad}} \sim 1\text{--}2$  that is typically observed in tokamaks and stellarators.<sup>28,48</sup> An average  $L_{\text{pol}}/L_{\text{rad}} = 1.5 \pm 0.1$  was reported for representative Ohmic NSTX discharges,<sup>69</sup> although larger ratios  $L_{\text{pol}}/L_{\text{rad}} \sim 3\text{--}4$  have been observed in some experiments<sup>80</sup> and simulations.<sup>12</sup>

There are two kinds of sheath-model boundary conditions that are commonly used in fluid and gyrokinetic codes. Logical-sheath boundary conditions enforce  $j_{\parallel} = 0$  at the sheath entrances, while current fluctuations into the sheath are permitted in conducting-sheath boundary conditions. Figure 12 shows the radial profiles of the steady-state parallel current into the sheath for the three cases under consideration. The currents have been normalized to peak steady-state ion saturation current  $j_{\text{sat}} = q_i n_i c_s$ , where  $c_s = \sqrt{(T_e + \gamma T_i)/m_i}$  and  $\gamma = 3$  is used because the collisionless layer in front of the sheaths should be resolved in all three cases. All three cases are quite quantitatively similar, and the outward sheath currents are found to be highly symmetric in  $z$ , which is consistent with the strong adiabatic response shown in Fig. 10. A large excess electron outflow (negative current) is seen in the hot source region (near  $x = 1.3 \text{ m}$ ), which is compensated by a large excess ion outflow (positive current) just outside the source region. The peak

values are approximately 20% of the ion saturation current, which motivates future studies regarding how the use of various sheath-model boundary conditions affect turbulence in these simulations.

#### IV. CONCLUSIONS

We have developed a model to investigate curvature-driven SOL turbulence in a simplified helical-magnetic-field geometry and performed numerical simulations of the system using an electrostatic gyrokinetic continuum code. The blobs in our simulations appear to originate as radially elongated structures that extend from the source region into the SOL and get broken up by sheared poloidal flows. The blobs appear to efficiently transport plasma across the magnetic field, leading to radial particle fluxes that are much higher than Bohm-flux estimates. Such large-amplitude and large-scale blobs were not observed in a set of simulations we performed without magnetic-curvature effects. We note, however, that coherent structures with high plasma density have been observed in linear devices with negligible magnetic curvature.<sup>81,82</sup> The mechanism that polarizes such coherent structures in linear devices and leads to outward radial propagation could be due to neutral wind.<sup>83</sup>

We characterized the turbulence using a variety of diagnostics and found that various quantities of interest are within the range expected for SOL turbulence in tokamaks, such as fluctuation levels, autocorrelation times, and correlation lengths. A summary of some quantities observed in our simulations is given in Table I, which also includes experimental values from the NSTX SOL.<sup>24,68</sup>

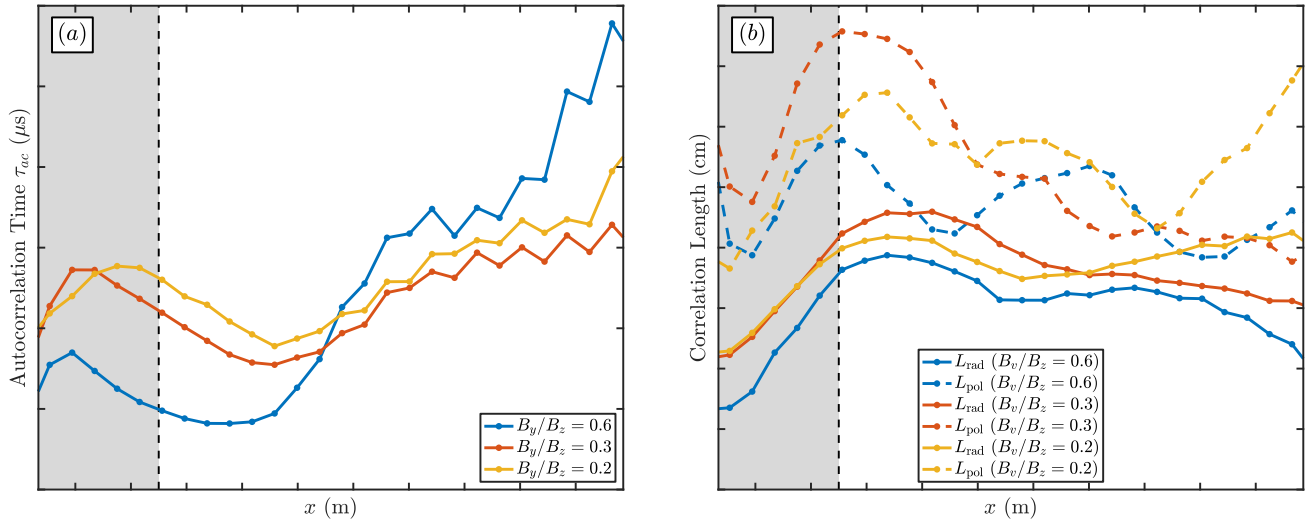


FIG. 11. Radial profiles of the (a) autocorrelation time and (b) poloidal (dashed lines) and radial (solid lines) correlation lengths computed at the  $z = 0$  m plane for three cases with different magnetic-field-line pitches. The shaded area indicates the region in which the source is concentrated.  $L_{\text{pol}}/L_{\text{rad}} \sim 1.2\text{--}1.6$  is observed across the radial domain.

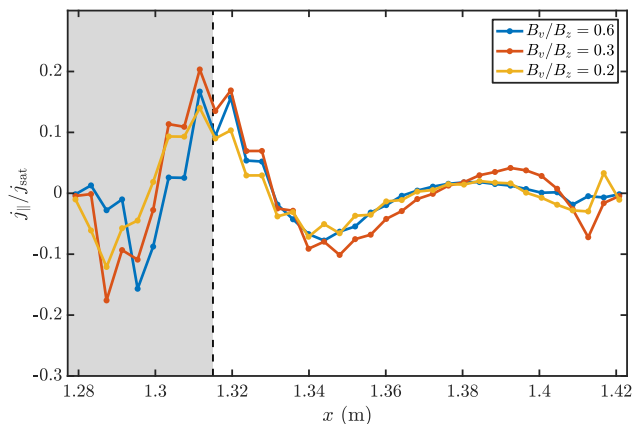


FIG. 12. Radial profiles of the steady-state parallel currents into the sheaths for cases with different magnetic-field-line pitches. The current is normalized to the peak value of the steady-state ion saturation current  $j_{\text{sat}} = q_i n_i c_s$  for each simulation. All three cases are quite quantitatively similar, featuring a large excess electron outflow in the source region that is balanced by a large excess ion outflow just outside of the source region.

We know that there are a number of important physical effects (e.g. complete magnetic geometry, magnetic fluctuations, and atomic physics) that need to be added to the simulations in order to expect quantitative accuracy for detailed comparisons with experiments, but it is interesting to see that the present simulations are already in the right ballpark qualitatively. This and other recent work indicate the general feasibility of using continuum codes to simulate gyrokinetic turbulence in the edge and SOL regions of tokamaks.

Even in this simple limit we began to explore a number of physical processes. We varied the magnetic-field-line pitch in a set of simulations, which indicated an increasing level of radial turbulent particle transport with decreasing pitch. A cross-coherence diagnostic comparing potential fluctuations at the sheaths with those at the midplane indicated that all three simulations appeared to fall into a similar turbulent regime with strongly adiabatic electrons. The application of this model to investigate turbulence in the Helimak device<sup>44,47</sup> has also been performed and will be reported elsewhere.

The helical-SOL model can be extended by the addition of a closed-magnetic-field-line region (with periodic boundary conditions in the parallel direction). While the Gkeyll code can already perform simulations with periodicity in the parallel direction, additional work is required to simultaneously include both open and closed-magnetic-field-line regions in the same simulation. The addition of good-magnetic-curvature regions and electromagnetic effects are also important extensions that will make this model more applicable to tokamaks. Since our model is relatively simple compared to a realistic tokamak SOL, the helical-SOL model could also eventually serve as a test case for the cross verification of gyrokinetic boundary-plasma codes. This test case might be useful for revealing major discrepancies due to different numerical approaches, sheath-model boundary conditions, and collision operators implemented in various codes relatively early on in the development cycle before more significant investments are made.

TABLE I. Summary of helical-SOL simulation results with comparison to experimental values for an H-mode NSTX SOL reported in Zweben *et al.*<sup>68</sup>. The values of  $\Gamma_{n,r}$ ,  $T_e$ , and  $n_e$  refer to values near the LCFS (the location of which is not precisely known in the experiments<sup>22</sup>). Since gas-puff imaging cannot be used to obtain particle fluxes, the value of  $\Gamma_{n,r}$  for the NSTX case is taken from Boedo *et al.*<sup>24</sup>. The ‘ $\sim$ ’ symbol is used here to indicate that there can be large variations in such quantities between discharges with different parameters. Ion temperature measurements in the plasma boundary of NSTX were not available, so the value of 1–2 (seen on the AUG and MAST tokamaks<sup>49</sup>) is assumed.

Quantity	Simulation Range	NSTX SOL
$\tau_{ac}$ ( $\mu\text{s}$ )	4–14	15–40
$L_{\text{pol}}$ (cm)	2–4	3–5
$L_{\text{rad}}$ (cm)	1–2.5	2–3
$\tilde{n}_{\text{rms}}/\bar{n}$ (%)	10–30	20–100
$\Gamma_{n,r}$ ( $10^{21} \text{ m}^{-2} \text{ s}^{-1}$ )	3.5–5.1	$\sim 4$
$n_e$ ( $10^{19} \text{ cm}^{-3}$ )	0.5–1.5	$\sim 1$
$T_e$ (eV)	26–29	$\sim 29$
$T_i/T_e$	1.5–2	1–2

## ACKNOWLEDGMENTS

We thank S. Zweben for useful discussions about NSTX SOL measurements and J. Juno for setting Gkeyll on the Stampede cluster. E. L. S. would also like to acknowledge useful discussions with J. Nichols concerning ion temperature measurements in the SOL and S. Zweben and M. Kunz for providing feedback on the manuscript. This work was funded by the U.S. Department of Energy under Contract DE-AC02-09CH11466, through the Max-Planck/Princeton Center for Plasma Physics and the Princeton Plasma Physics Laboratory. E. L. S. prepared this manuscript in part under the auspices of the U.S. Department of Energy by Lawrence Livermore National Laboratory under Contract DE-AC52-07NA27344. G. W. H. and A. H. were supported in part by the SciDAC Partnership for Multiscale Gyrokinetic Turbulence. A. H. was also supported in part by the Laboratory Directed Research and Development program. Some simulations reported in this paper were performed on the Perseus cluster at the TIGRESS high performance computer center at Princeton University, which is jointly supported by the Princeton Institute for Computational Science and Engineering and the Princeton University Office of Information Technology’s Research Computing department. This work also used the Extreme Science and Engineering Discovery Environment (XSEDE), which is supported by National Science Foundation grant number ACI-1548562.

## Appendix A: Initial Conditions

We consider a problem in which a uniform mass source  $S_\rho$  and energy source  $S_E$  is continuously active in the region  $|z| < L_S/2$ . This fluid flows out to perfectly absorbing boundaries at  $|z| = L_S/2$ . We treat the plasma as a single fluid with mass density  $\rho \approx n_e m_i$ , pressure  $p = n_e(T_e + T_i) = 2n_e T$  (where  $T$  is an average of the electron and ion temperatures), and energy density  $(3/2)n_e(T_e + T_i)$ , so  $S_\rho = m_i S_n$  and  $S_E = 3T_{\text{src}} S_n$ , where  $S_n$  is the electron and ion particle source rate and  $T_{\text{src}} = (T_{e,\text{src}} + T_{i,\text{src}})/2$  is the effective single-fluid source temperature. This system is described by the steady-state ideal fluid equations (neglecting thermal conduction and viscosity)

$$0 = -\frac{\partial}{\partial z}(\rho u) + S_\rho, \quad (\text{A1})$$

$$0 = -\frac{\partial}{\partial z}(\rho u^2 + p), \quad (\text{A2})$$

$$0 = -\frac{\partial}{\partial z}\left(\frac{1}{2}\rho u^3 + \frac{5}{2}pu\right) + S_E, \quad (\text{A3})$$

where  $u$  is the fluid velocity,  $\rho$  is the mass density, and  $p$  is the pressure. We treat the source as having no mean flow in the  $z$  direction.

We integrate these equations from  $z = 0$  to an arbitrary position  $z < L_S/2$  and use the boundary condition  $u(z = 0) = 0$  to get

$$\rho u = S_\rho z, \quad (\text{A4})$$

$$\rho u^2 + p = p_0, \quad (\text{A5})$$

$$\frac{1}{2}\rho u^3 + \frac{5}{2}pu = zS_E, \quad (\text{A6})$$

where  $p_0 \equiv p(z = 0)$ . The first two equations can be solved for  $\rho$  and  $p$  respectively, and we obtain a quadratic equation for  $u(z)$  by substituting these expressions into the last equation. The solution to this system is

$$p(z) = \frac{3p_0 \mp \sqrt{25p_0^2 - 32z^2 S_\rho S_E}}{8}, \quad (\text{A7})$$

$$u(z) = \frac{5p_0 \pm \sqrt{25p_0^2 - 32z^2 S_\rho S_E}}{8S_\rho z}, \quad (\text{A8})$$

$$\rho(z) = \frac{zS_\rho}{u}. \quad (\text{A9})$$

Since the pressure cannot be negative, the only physical solution for small  $z$  is the negative branch for  $u(z)$  and the positive branch for  $p(z)$ . The central pressure  $p_0$  is determined by the boundary conditions at  $|z| = L_S/2$ . A steady-state solution at a perfectly absorbing wall requires  $\mathcal{M} \geq 1$  at the wall,<sup>84</sup> where the Mach number  $\mathcal{M}(z) \equiv u(z)/c_s(z) = u(z)/\sqrt{(5/3)p(z)/\rho(z)}$ . The  $\mathcal{M} \geq 1$  requirement is equivalent to the Bohm criterion for a steady-state sheath. We see that

$$\mathcal{M}(z)^2 = \frac{\rho(z)u(z)^2}{(5/3)p(z)^2} = \frac{3}{5} \frac{p_0 - p}{p}. \quad (\text{A10})$$

The maximum possible value of  $\mathcal{M}(z)$  occurs at the  $z$  that minimizes  $p(z)$ . This value  $z_{\max}$  turns out to be the  $z$  that makes the radicand in Eq. (A7) zero, so we find that

$$z_{\max}^2 = \frac{25}{32} \frac{p_0^2}{S_p S_E}, \quad (\text{A11})$$

$$p(z_{\max}) = \frac{3}{8} p_0, \quad (\text{A12})$$

$$\mathcal{M}(z_{\max}) = 1. \quad (\text{A13})$$

This says that the largest possible value of  $\mathcal{M}$  is 1 [when  $z$  has been made as large as possible, as given by Eq. (A11)]. This (barely) satisfies the outflow requirement that  $\mathcal{M} \geq 1$  at a perfectly absorbing wall. Equation (A11) then provides a constraint on the value of  $p_0$  such that  $\mathcal{M} = 1$  is achieved at the end of the source region,  $z_{\max} = L_S/2$ :

$$p_0 = \frac{L_S}{2} \sqrt{\frac{32}{25} S_p S_E}. \quad (\text{A14})$$

Using this expression for  $p_0$ , we have the following profiles in the source region  $0 < |z| < L_S/2$ :

$$p(z) = p_0 \left( \frac{3 + 5\sqrt{1 - z^2/(L_S/2)^2}}{8} \right), \quad (\text{A15})$$

$$u(z) = \frac{\sqrt{3}}{2} \sqrt{\frac{2T_{\text{src}}}{m_i}} \left( \frac{1 - \sqrt{1 - z^2/(L_S/2)^2}}{z/(L_S/2)} \right), \quad (\text{A16})$$

$$\rho(z) = \frac{16S_p^2}{5p_0} \left( \frac{L_S}{2} \right)^2 \left( \frac{1 + \sqrt{1 - z^2/(L_S/2)^2}}{2} \right) \quad (\text{A17})$$

In order to use these profiles to initialize a Maxwellian initial condition for a kinetic simulation, we note that these profiles correspond to density ( $n = \rho/m_i$ ) and temperature ( $T = m_i p/(2\rho)$ ) profiles in the source region given by

$$T(z) = \frac{3}{5} T_{\text{src}} \left( \frac{3 + 5\sqrt{1 - z^2/(L_S/2)^2}}{4 + 4\sqrt{1 - z^2/(L_S/2)^2}} \right), \quad (\text{A18})$$

$$n(z) = \frac{4\sqrt{5}}{3} \frac{(L_S/2) S_n}{c_{\text{ss}}} \left( \frac{1 + \sqrt{1 - z^2/(L_S/2)^2}}{2} \right) \quad (\text{A19})$$

where  $c_{\text{ss}} = \sqrt{(5/3)2T_{\text{src}}/m_i}$ . In the source-free regions  $z > L_S/2$  or  $z < -L_S/2$ ,  $n(z)$ ,  $T(z)$ , and  $u(z)$  are all constant and equal to the value that their respective profiles evaluated at the corresponding edge of the source region at  $z = L_S/2$  or  $z = -L_S/2$ . The 1-D equilibrium profiles Eqs. (A16), (A18), and (A19), the density source in the helical-SOL simulations Eq. (5), and the temperature profiles of the electron and ion sources are used to generate spatially varying initial conditions in  $(x, y, z)$ .

One could go further by calculating the slight difference between the ion-guiding-center-density and electron-density profiles that gives the desired equilibrium potential  $\phi(x, y, z)$  when the gyrokinetic Poisson equation is solved. For now, we simply set  $n_i^g(x, y, z) = n_e(x, y, z)$  and initialize with  $\phi = 0$ , as we did in the LAPD simulations of Shi *et al.*<sup>14</sup>.

<sup>1</sup>R. H. Cohen and X. Q. Xu, *Contrib. Plasma Phys.* **48**, 212 (2008).

<sup>2</sup>P. Ricci, *J. Plasma Phys.* **81** (2015), [10.1017/S0022377814001202](https://doi.org/10.1017/S0022377814001202).

<sup>3</sup>B. D. Scott, A. Kendl, and T. Ribeiro, *Contrib. Plasma Phys.* **50**, 228 (2010).

<sup>4</sup>B. D. Scott, *Plasma Phys. Controlled Fusion* **45**, A385 (2003).

<sup>5</sup>T. Eich, A. W. Leonard, R. A. Pitts, W. Fundamenski, R. J. Goldston, T. K. Gray, A. Herrmann, A. Kirk, A. Kallenbach, O. Kardaun, A. S. Kukushkin, B. LaBombard, R. Maingi, M. A. Makowski, A. Scarabosio, B. Sieglin, J. Terry, A. Thornton, AS-DEX Upgrade Team, and JET EFDA Contributors, *Nucl. Fusion* **53**, 093031 (2013).

<sup>6</sup>R. Goldston, *Nucl. Fusion* **52**, 013009 (2012).

<sup>7</sup>C. S. Chang, S. Ku, A. Loarte, V. Parail, F. Köchl, M. Romanelli, R. Maingi, J.-W. Ahn, T. Gray, J. Hughes, B. LaBombard, T. Leonard, M. Makowski, and J. Terry, *Nucl. Fusion* **57**, 116023 (2017).

<sup>8</sup>F. Wagner, *Plasma Phys. Controlled Fusion* **49**, B1 (2007).

<sup>9</sup>F. Wagner, G. Becker, K. Behringer, D. Campbell, A. Eberhagen, W. Engelhardt, G. Fussmann, O. Gehre, J. Gernhardt, G. v. Gierke, G. Haas, M. Huang, F. Karger, M. Keilhacker, O. Klüber, M. Kornherr, K. Lackner, G. Lisitano, G. G. Lister, H. M. Mayer, D. Meisel, E. R. Müller, H. Murmann, H. Niedermeyer, W. Poschenrieder, H. Rapp, H. Röhr, F. Schneider, G. Siller, E. Speth, A. Stäbler, K. H. Steuer, G. Venus, O. Vollmer, and Z. Yü, *Phys. Rev. Lett.* **49**, 1408 (1982).

<sup>10</sup>M. Kotschenreuther, W. Dorland, M. A. Beer, and G. W. Hammett, *Phys. Plasmas* **2**, 2381 (1995).

<sup>11</sup>J. Kinsey, G. Staebler, J. Candy, R. Waltz, and R. Budny, *Nucl. Fusion* **51**, 083001 (2011).

<sup>12</sup>R. M. Churchill, C. S. Chang, S. Ku, and J. Dominski, *Plasma Phys. Controlled Fusion* **59**, 105014 (2017).

<sup>13</sup>T. Korpilo, A. D. Gurchenko, E. Z. Gusakov, J. A. Heikkinen, S. J. Janhunen, T. P. Kiviniemi, S. Leerink, P. Niskala, and A. A. Perevalov, *Comput. Phys. Commun.* **203**, 128 (2016).

<sup>14</sup>E. L. Shi, G. W. Hammett, T. Stoltzfus-Dueck, and A. Hakim, *J. Plasma Phys.* **83**, 905830304 (2017).

<sup>15</sup>E. L. Shi, *Gyrokinetic continuum simulation of turbulence in open-field-line plasmas*, Ph.D. thesis, Princeton University (2017).

<sup>16</sup>Q. Pan, D. Told, E. L. Shi, G. W. Hammett, and F. Jenko, *Phys. Plasmas* **25**, 062303 (2018).

<sup>17</sup>M. A. Dorf, M. R. Dorr, J. A. Hittinger, R. H. Cohen, and T. D. Rognlien, *Phys. Plasmas* **23**, 056102 (2016), [10.1063/1.4943106](https://doi.org/10.1063/1.4943106).

<sup>18</sup>Q. Pan, D. Told, and F. Jenko, *Phys. Plasmas* **23**, 102302 (2016).

<sup>19</sup>J. A. Krommes, *Annu. Rev. Fluid Mech.* **44**, 175 (2012).

<sup>20</sup>C. S. Chang, S. Ku, P. H. Diamond, Z. Lin, S. Parker, T. S. Hahm, and N. Samatova, *Phys. Plasmas* **16**, 056108 (2009), [10.1063/1.3099329](https://doi.org/10.1063/1.3099329).

<sup>21</sup>P. C. Stangeby, *The plasma boundary of magnetic fusion devices*, Plasma physics series (Taylor & Francis, New York, 2000).

<sup>22</sup>S. J. Zweben, R. J. Maqueda, D. P. Stotler, A. Keesee, J. Boedo, C. E. Bush, S. M. Kaye, B. LeBlanc, J. L. Lowrance, V. J. Mastromicola, R. Maingi, N. Nishino, G. Renda, D. W. Swain, J. B. Wilgen, and the NSTX Team, *Nucl. Fusion* **44**, 134 (2004).

<sup>23</sup>J. L. Terry, B. LaBombard, B. Lipschultz, M. J. Greenwald, J. E. Rice, and S. J. Zweben, *Fusion Sci. Technol.* **51**, 342 (2007).

<sup>24</sup>J. A. Boedo, J. R. Myra, S. Zweben, R. Maingi, R. J. Maqueda, V. A. Soukhanovskii, J. W. Ahn, J. Canik, N. Crocker, D. A. D'Ippolito, R. Bell, H. Kugel, B. Leblanc, L. A. Roquemore, and D. L. Rudakov, *Phys. Plasmas* **21**, 042309 (2014).



- <sup>25</sup>S. J. Zweben, *Phys. Fluids* **28**, 974 (1985).
- <sup>26</sup>S. J. Zweben and R. W. Gould, *Nucl. Fusion* **25**, 171 (1985).
- <sup>27</sup>D. A. D'Ippolito, J. R. Myra, and S. J. Zweben, *Phys. Plasmas* **18**, 060501 (2011).
- <sup>28</sup>S. J. Zweben, J. A. Boedo, O. Grulke, C. Hidalgo, B. LaBombard, R. J. Maqueda, P. Scarin, and J. L. Terry, *Plasma Phys. Controlled Fusion* **49**, S1 (2007).
- <sup>29</sup>V. Naulin, *J. Nucl. Mater.* **363**, 24 (2007).
- <sup>30</sup>S. I. Krasheninnikov, *Phys. Lett. A* **283**, 368 (2001).
- <sup>31</sup>J. R. Myra, D. A. D'Ippolito, S. I. Krasheninnikov, and G. Q. Yu, *Phys. Plasmas* **11**, 4267 (2004).
- <sup>32</sup>J. R. Angus, M. V. Umansky, and S. I. Krasheninnikov, *Phys. Rev. Lett.* **108**, 215002 (2012).
- <sup>33</sup>F. Riva, C. Colin, J. Denis, L. Easy, I. Furno, J. Madsen, F. Militello, V. Naulin, A. H. Nielsen, J. M. B. Olsen, J. T. Omotani, J. J. Rasmussen, P. Ricci, E. Serre, P. Tamain, and C. Theiler, *Plasma Phys. Controlled Fusion* **58**, 044005 (2016).
- <sup>34</sup>N. R. Walkden, B. D. Dudson, L. Easy, G. Fishpool, and J. T. Omotani, *Nucl. Fusion* **55**, 113022 (2015).
- <sup>35</sup>B. W. Shanahan and B. D. Dudson, *Plasma Phys. Controlled Fusion* **58**, 125003 (2016).
- <sup>36</sup>N. Bisai, A. Das, S. Deshpande, R. Jha, P. Kaw, A. Sen, and R. Singh, *Phys. Plasmas* **12**, 102515 (2005).
- <sup>37</sup>Y. Sarazin, P. Ghendrih, G. Attuel, C. Clément, X. Garbet, V. Grandgirard, M. Ottaviani, S. Benkadda, P. Beyer, N. Bian, and C. Figarella, *J. Nucl. Mater.* **313–316**, 796 (2003).
- <sup>38</sup>O. E. Garcia, J. Horacek, R. A. Pitts, A. H. Nielsen, W. Fundamenski, J. P. Graves, V. Naulin, and J. J. Rasmussen, *Plasma Phys. Controlled Fusion* **48**, L1 (2006).
- <sup>39</sup>P. Ricci and B. N. Rogers, *Phys. Plasmas* **20**, 010702 (2013).
- <sup>40</sup>A. Stegmeir, D. Coster, A. Ross, O. Maj, K. Lackner, and E. Poli, *Plasma Phys. Controlled Fusion* **60**, 035005 (2018).
- <sup>41</sup>C. Baudoin, P. Tamain, H. Bufferand, G. Ciraolo, N. Fedorcak, D. Galassi, P. Ghendrih, and N. Nace, *Contrib. Plasma Phys.* **58**, 484 (2018).
- <sup>42</sup>W. Gekelman, P. Pribyl, Z. Lucky, M. Drandell, D. Leneman, J. Maggs, S. Vincena, B. V. Compernelle, S. K. P. Tripathi, G. Morales, T. A. Carter, Y. Wang, and T. DeHaas, *Rev. Sci. Instrum.* **87**, 025105 (2016).
- <sup>43</sup>A. Fasoli, B. Labit, M. McGrath, S. H. Müller, G. Plyushchev, M. Podestà, and F. M. Poli, *Phys. Plasmas* **13**, 055902 (2006).
- <sup>44</sup>K. W. Gentle and H. He, *Plasma Sci. Tech.* **10**, 284 (2008).
- <sup>45</sup>P. Ricci, B. N. Rogers, and S. Brunner, *Phys. Rev. Lett.* **100**, 225002 (2008).
- <sup>46</sup>P. Ricci and B. N. Rogers, *Phys. Plasmas* **16**, 092307 (2009), 10.1063/1.3230119.
- <sup>47</sup>B. Li, B. N. Rogers, P. Ricci, K. W. Gentle, and A. Bhattacharjee, *Phys. Rev. E* **83**, 056406 (2011).
- <sup>48</sup>J. A. Boedo, N. Crocker, L. Chousal, R. Hernandez, J. Chalfant, H. Kugel, P. Roney, and J. Wertenbaker, *Rev. Sci. Instrum.* **80**, 123506 (2009).
- <sup>49</sup>M. Kočan, J. Gunn, S. Carpentier-Chouchana, A. Herrmann, A. Kirk, M. Komm, H. Miller, J.-Y. Pascal, R. Pitts, V. Rohde, and P. Tamain, *J. Nucl. Mater.* **415**, S1133 (2011).
- <sup>50</sup>M. Kočan, F. P. Genrich, A. Kendl, H. W. Müller, and the ASDEX Upgrade Team, *Plasma Phys. Controlled Fusion* **54**, 085009 (2012).
- <sup>51</sup>F. D. Halpern, P. Ricci, S. Jolliet, J. Loizu, J. Morales, A. Masetto, F. Musil, F. Riva, T. M. Tran, and C. Wersal, *J. Comput. Phys.* **315**, 388 (2016).
- <sup>52</sup>B. Zhu, M. Francisquez, and B. N. Rogers, *Phys. Plasmas* **24**, 055903 (2017).
- <sup>53</sup>T. T. Ribeiro and B. Scott, *Plasma Phys. Controlled Fusion* **47**, 1657 (2005).
- <sup>54</sup>S. J. Zweben, B. D. Scott, J. L. Terry, B. LaBombard, J. W. Hughes, and D. P. Stotler, *Phys. Plasmas* **16**, 082505 (2009).
- <sup>55</sup>B. D. Dudson and J. Leddy, *Plasma Phys. Controlled Fusion* **59**, 054010 (2017).
- <sup>56</sup>M. Francisquez, B. Zhu, and B. N. Rogers, *Nucl. Fusion* **57**, 116049 (2017).
- <sup>57</sup>M. A. Beer, S. C. Cowley, and G. W. Hammett, *Phys. Plasmas* **2**, 2687 (1995).
- <sup>58</sup>G. W. Hammett, M. A. Beer, W. Dorland, S. C. Cowley, and S. A. Smith, *Plasma Phys. Controlled Fusion* **35**, 973 (1993).
- <sup>59</sup>B. Scott, *Phys. Plasmas* **5**, 2334 (1998).
- <sup>60</sup>A. J. Brizard and T. S. Hahm, *Rev. Mod. Phys.* **79**, 421 (2007).
- <sup>61</sup>H. Sugama, *Phys. Plasmas* **7**, 466 (2000).
- <sup>62</sup>Y. Idomura, H. Urano, N. Aiba, and S. Tokuda, *Nucl. Fusion* **49**, 065029 (2009).
- <sup>63</sup>A. Lenard and I. B. Bernstein, *Phys. Rev.* **112**, 1456 (1958).
- <sup>64</sup>P. Ricci and B. N. Rogers, *Phys. Rev. Lett.* **104**, 145001 (2010).
- <sup>65</sup>S. E. Parker, R. J. Procassini, C. K. Birdsall, and B. I. Cohen, *J. Comput. Phys.* **104**, 41 (1993).
- <sup>66</sup>E. L. Shi, A. H. Hakim, and G. W. Hammett, *Phys. Plasmas* **22**, 022504 (2015).
- <sup>67</sup>L. Chôné, T. Kiviniemi, S. Leerink, P. Niskala, and R. Rochford, *Contrib. Plasma Phys.* **58**, 534.
- <sup>68</sup>S. J. Zweben, W. M. Davis, S. M. Kaye, J. R. Myra, R. E. Bell, B. P. LeBlanc, R. J. Maqueda, T. Munsat, S. A. Sabbagh, Y. Sechrest, D. P. Stotler, and the NSTX Team, *Nucl. Fusion* **55**, 093035 (2015).
- <sup>69</sup>S. J. Zweben, J. R. Myra, W. M. Davis, D. A. D'Ippolito, T. K. Gray, S. M. Kaye, B. P. LeBlanc, R. J. Maqueda, D. A. Russell, D. P. Stotler, and the NSTX-U Team, *Plasma Phys. Controlled Fusion* **58**, 044007 (2016).
- <sup>70</sup>R. Chodura, *Phys. Fluids* **25**, 1628 (1982).
- <sup>71</sup>J.-G. Liu and C.-W. Shu, *J. Comput. Phys.* **160**, 577 (2000).
- <sup>72</sup>S. Gottlieb, C.-W. Shu, and E. Tadmor, *SIAM Rev.* **43**, 89 (2001).
- <sup>73</sup>M. A. Makowski, D. Elder, T. K. Gray, B. LaBombard, C. J. Lasnier, A. W. Leonard, R. Maingi, T. H. Osborne, P. C. Stangeby, J. L. Terry, and J. Watkins, *Phys. Plasmas* **19**, 056122 (2012).
- <sup>74</sup>S. I. Krasheninnikov, D. A. D'Ippolito, and J. R. Myra, *J. Plasma Phys.* **74**, 679 (2008).
- <sup>75</sup>J. A. Krommes, *Phys. Plasmas* **15**, 030703 (2008).
- <sup>76</sup>P. C. Stangeby and G. M. McCracken, *Nucl. Fusion* **30**, 1225 (1990).
- <sup>77</sup>B. D. Scott, *Phys. Plasmas* **12**, 062314 (2005).
- <sup>78</sup>A. Masetto, F. D. Halpern, S. Jolliet, J. Loizu, and P. Ricci, *Phys. Plasmas* **20**, 092308 (2013).
- <sup>79</sup>T. Stoltzfus-Dueck, *Tokamak edge turbulence and the approach to adiabatic response*, Ph.D. thesis, Princeton University (2009).
- <sup>80</sup>A. Huber, U. Samm, B. Schweer, and P. Mertens, *Plasma Phys. Controlled Fusion* **47**, 409 (2005).
- <sup>81</sup>G. Y. Antar, S. I. Krasheninnikov, P. Devynck, R. P. Doerner, E. M. Hollmann, J. A. Boedo, S. C. Luckhardt, and R. W. Conn, *Phys. Rev. Lett.* **87**, 065001 (2001).
- <sup>82</sup>T. A. Carter, *Phys. Plasmas* **13**, 010701 (2006), 10.1063/1.2158929.
- <sup>83</sup>S. I. Krasheninnikov and A. I. Smolyakov, *Phys. Plasmas* **10**, 3020 (2003).
- <sup>84</sup>C.-D. Munz, *Math Methods Appl Sci* **17**, 597 (1994).